

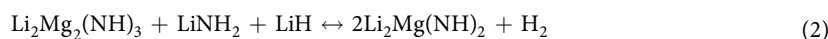
OPEN

Improved kinetic behaviour of $\text{Mg}(\text{NH}_2)_2\text{-2LiH}$ doped with nanostructured K-modified- $\text{Li}_x\text{Ti}_y\text{O}_z$ for hydrogen storage

Gökhan Gizer^{1*}, Julián Puzskiel^{1,2}, Maria Victoria Castro Riglos^{1,2}, Claudio Pistidda^{1*}, José Martín Ramallo-López³, Martín Mizrahi³, Antonio Santoru¹, Thomas Gemming⁴, Jo-Chi Tseng⁵, Thomas Klassen¹ & Martin Dornheim^{1*}

The system $\text{Mg}(\text{NH}_2)_2 + 2\text{LiH}$ is considered as an interesting solid-state hydrogen storage material owing to its low thermodynamic stability of ca. 40 kJ/mol H_2 and high gravimetric hydrogen capacity of 5.6 wt.%. However, high kinetic barriers lead to slow absorption/desorption rates even at relatively high temperatures (>180 °C). In this work, we investigate the effects of the addition of K-modified $\text{Li}_x\text{Ti}_y\text{O}_z$ on the absorption/desorption behaviour of the $\text{Mg}(\text{NH}_2)_2 + 2\text{LiH}$ system. In comparison with the pristine $\text{Mg}(\text{NH}_2)_2 + 2\text{LiH}$, the system containing a tiny amount of nanostructured K-modified $\text{Li}_x\text{Ti}_y\text{O}_z$ shows enhanced absorption/desorption behaviour. The doped material presents a sensibly reduced (~30 °C) desorption onset temperature, notably shorter hydrogen absorption/desorption times and reversible hydrogen capacity of about 3 wt. % H_2 upon cycling. Studies on the absorption/desorption processes and micro/nanostructural characterizations of the $\text{Mg}(\text{NH}_2)_2 + 2\text{LiH} + \text{K-modified } \text{Li}_x\text{Ti}_y\text{O}_z$ system hint to the fact that the presence of *in situ* formed nanostructure K_2TiO_3 is the main responsible for the observed improved kinetic behaviour.

One of the limiting factors for the implementation of hydrogen in stationary and mobile applications is the lack of an efficient and safe storage system. For mobile applications, a fuel cell equipped electrical car requires about 5 kg of hydrogen in order to achieve a driving range of ca. 500 km¹. However, storing 5 kg of hydrogen in a high-pressure (700 bar) tank requires an internal volume of 122 litres². In order to improve the volumetric hydrogen storage capacity, solid-state storage in metal hydrides is considered as an effective approach^{3–8}. As an example, excluding the volume of the tank material, 5 kg of hydrogen can be stored in magnesium hydride (MgH_2) occupying a volume of only 46 litres⁷. However, due to its high desorption enthalpy ($\Delta H_{des} = 74 \text{ kJ mol}^{-1}$), MgH_2 requires high dehydrogenation temperatures (>300 °C)⁹. By the reaction of alkali metals (i.e. Na, K) with gaseous ammonia, metal amides (i.e. NaNH_2 and KNH_2) were firstly discovered at the beginning of 1800s^{10,11}. During the last 50 years, metal amides were not considered as potential hydrogen storage materials since the detected main gaseous product from their thermal decomposition was ammonia^{12,13}. In 2002, Chen *et al.* reported for the first time that a material composed of LiNH_2 and LiH was able to reversibly store 6.5 wt. % of H_2 at 255 °C¹⁴. Thereafter, a focus was given to synthesize and understand the mechanisms in amide-imide systems for hydrogen storage^{15,16}. Replacing LiNH_2 with $\text{Mg}(\text{NH}_2)_2$, a reversible H_2 storage capacity of 5.5 wt. % at operating temperatures of 200 °C is obtained according to reactions (1) and (2) ($\Delta H_{des} = 40 \text{ kJ mol}^{-1}$)¹⁷.



¹Institute of Materials Research, Materials Technology, Helmholtz-Zentrum Geesthacht GmbH, Max-Planck Strasse 1, D-21502, Geesthacht, Germany. ²Consejo Nacional de Investigaciones Científicas y Técnicas (CONICET), Centro Atómico Bariloche, Av. Bustillo km 9500, S.C. de Bariloche, Argentina. ³Instituto de Investigaciones Físicoquímicas Teóricas y Aplicadas, INIFTA (CCT La Plata-CONICET, UNLP), Diagonal 113 y Calle 64, 1900, La Plata, Argentina. ⁴IFW Dresden, P.O. Box 270016, D-01171, Dresden, Germany. ⁵Deutsches elektronen-Synchrotron, Notkestr. 85, 22607, Hamburg, Germany. *email: goekhan.gizer@hzg.de; claudio.pistidda@hzg.de; martin.dornheim@hzg.de

Sample composition	Sample code
Mg(NH ₂) ₂ + 2LiH	Mg-Li
Mg(NH ₂) ₂ + 2LiH + 0.05(0.5LiH + TiO ₂)	Mg-Li-5LTO
Mg(NH ₂) ₂ + 2LiH + 0.05(0.5LiH + TiO ₂ + 0.25KH)	Mg-Li-5LTOK
Mg(NH ₂) ₂ + 2LiH + 0.025(0.5LiH + TiO ₂ + 0.25KH)	Mg-Li-2.5LTOK
Mg(NH ₂) ₂ + 2LiH + 0.010(0.5LiH + TiO ₂ + 0.25KH)	Mg-Li-1LTOK
Mg(NH ₂) ₂ + 2LiH + 0.05KH	Mg-Li-5K

Table 1. Compositions and designations for the investigated samples.

According to the calculated thermodynamic properties of the Mg(NH₂)₂ + 2LiH stoichiometric mixture, operating temperatures of 90 °C can be achieved at 1 bar¹⁸. However, sufficient dehydrogenation rates, even after intense ball milling treatment, can be obtained only at temperatures above 180 °C due to harsh kinetic constraints¹⁹. Several attempts have been made in order to improve the sluggish dehydrogenation behaviour of the Mg(NH₂)₂ + 2LiH composite system^{18–39}. Potassium containing additives effectively reduce the dehydrogenation peak temperature down to 130 °C, which is ~50 °C lower than that of pristine Mg(NH₂)₂ + 2LiH^{40–42}. However, due to segregation phenomena that occurs at high-temperature (≥180 °C) upon cycling, the inhomogeneous distribution of the K-species reduces their catalytic activity⁴³. Therefore, the design/synthesis of new additives is mandatory in order to achieve long-lasting absorption/desorption properties. TiO₂ is one of the low-cost additives which enhance the hydrogen storage properties of the 2LiBH₄ + MgH₂ reactive hydride composite (RHC) system^{44–46}. Puzkiel *et al.* showed that 2LiH + MgB₂/2LiBH₄ + MgH₂ RHC system doped with core-shell Li_xTiO₂ nanoparticles shows improved the kinetic and cycling behaviour⁴⁴. It was found that the core-shell Li_xTiO₂ nanoparticles act as Li⁺ pumps, increasing Li⁺ mobility, hence accounting for the observed enhanced hydrogen storage properties. Studies on reaction mechanism of Mg(NH₂)₂ + LiH system showed that diffusion of small ions (e.g., Li⁺, Mg⁺², and H⁺) might account for the improved reaction kinetics^{47–50}. In this work, we investigate the effect of Li_xTi_yO_z and potassium-modified Li_xTi_yO_z additives on the microstructural and hydrogen storage properties of Mg(NH₂)₂ + 2LiH system.

Experimental

Additive synthesis. All reagents utilized in this work were Mg(NH₂)₂ (described in the following subsection), LiH (Alfa Aesar, 97 % purity), anatase TiO₂ (Sigma Aldrich, >99 % purity, - 325 mesh) and KH (Sigma Aldrich, suspension 35% in mineral oil). The investigated additives were obtained by milling LiH, TiO₂ and KH in different stoichiometric ratios under argon atmosphere for two hours and then annealing them under Ar atmosphere at 600 °C for 8 hours. The stoichiometry of the reagent utilized to synthesize the additives were: 1) 0.5LiH + TiO₂ and 2) 0.5LiH + TiO₂ + 0.25KH. In addition to the prepared additives, KH alone was also used as an additive. In order to separate mineral oil from KH, three washing cycles in hexane were carried out. After that, hexane was removed by applying dynamic vacuum.

Material synthesis. Mg(NH₂)₂ (95 % purity) was *in-house* synthesized by ball milling MgH₂ under NH₃ atmosphere, followed by annealing at 300 °C under NH₃ atmosphere. The details of the synthesis were described in our previous study⁵⁰. The Mg(NH₂)₂ was mixed with LiH (Alfa Aesar, 97 % purity) and 1.0, 2.5 or 5 mol. % of additives (Section 2.2). All materials were milled in a Fritsch P6 Planetary ball miller for 5 hours with ball to powder ratio 60:1 under 50 bar of H₂ pressure. The sample names used to identify the prepared specimens are listed in Table 1.

Characterization techniques. *Ex situ* powder X-ray diffraction method (PXD) was applied for the identification of crystalline phases, by using a Bruker D8 Discover diffractometer equipped with Cu X-ray source (λ = 1.54 Å) operating at 50 kV and 1000 mA and a 2D VANTEC detector. Diffraction patterns were collected in the 2θ range 20° to 80°. A sample holder sealed with a polymethylmethacrylate (PMMA) dome was utilized to prevent the material oxidation during PXD measurements.

In situ synchrotron radiation powder X-ray diffraction (SR-PXD) technique was applied using a special designed cell⁵¹. This cell with sapphire capillary allows performing measurements under controlled gas atmosphere in a pressure range from 0.01 to 200 bar. Measurements were performed at Deutsches Elektronen-Synchrotron (DESY) in the P02.1 beamline. The beamline is equipped with A Perkin Elmer XRD1621 area detector and 60 keV X-ray source (λ = 0.207 Å). Mg-Li-5LTOK sample was heated from room temperature (RT) to 300 °C with a heating rate of 5 °C/min under 1 bar of H₂ pressure. Every 10 seconds a two-dimensional SR-PXD pattern was collected. Collected data were integrated to one-dimensional diffraction pattern using Fit2D software^{52,53}.

Differential scanning calorimetry (DSC) measurements were performed in a Netzsch DSC 204 HP calorimeter located inside an argon-filled glovebox (H₂O and O₂ levels below 1 ppm). Before starting the DSC measurements, the residual argon gas inside the chamber was removed by first evacuation and then flushing the chamber with hydrogen. A mass flow-meter was used to limit the deviation of the hydrogen pressure to ±0.2 bar of H₂ during heating up and cooling down. In order to measure apparent activation energies of the 1st and 2nd desorption, about 10–15 mg of each sample were placed in a Al₂O₃ crucible and then heated from room temperature (RT) up to 300 °C under 1 bar of H₂ pressure with heating rates of 1 °C, 3 °C, 5 °C and 10 °C/min. For the 2nd desorption,

as-milled samples were first desorbed by heating from RT to 220 °C under 1 bar of H₂ pressure. Following this step, the materials were reabsorbed by heating them from RT to 180 °C under 100 bar of H₂ pressure.

In order to evaluate the effectiveness of the additives on the material kinetic behaviour, the apparent activation energies (E_a) of the 1st and 2nd desorption reactions were calculated *via* Kissinger method⁵⁴. This method is suitable for the samples that exhibit multi-step reactions and it allows us to determine E_a of a reaction process without assuming a specific kinetic model, i.e. without determining the rate-limiting step of the reaction. The equation for the E_a calculation is shown in Eq. 3;

$$\ln(\beta/T_m^2) = \ln(AR/E_a) - \frac{E_a}{RT_m}, \quad (3)$$

where A is the pre-exponential factor and R is the gas constant. The temperature for the maximum reaction rate (T_m) was obtained from DSC curves measured at measured heating rates (β) of 1 °C, 3 °C, 5 °C and 10 °C/min. Then, $\ln\left(\frac{\beta}{T_m^2}\right)$ against $1/T_m$ was plotted, E_a (kJ/mol H₂) and A (1/s) was calculated from linear fitting. Goodness of fit was determined by the examining the correlation between the experimental and predicted values. In order to have a good fitting, R-square value should be near 1⁵⁰.

In order to assess the rate-limiting steps of the absorption/desorption processes in the studied system, Sharp and Jones method was applied^{55,56}. In this method, experimental data are expressed as following:

$$F(\alpha) = A \left(\frac{t}{t_{0.5}} \right), \quad (4)$$

where A is the rate constant, $t_{0.5}$ is the time at the reaction fraction $\alpha = 0.5$. The fraction (α) is taken as the hydrogen capacity over the maximum reached capacity for each sample. By implementing different rate equations, several plots of $\left(\frac{t}{t_{0.5}}\right)_{\text{theoretical}}$ versus $\left(\frac{t}{t_{0.5}}\right)_{\text{experimental}}$ are obtained. In this study, we applied this model to the 1st, 2nd and 5th absorption/desorption curves between 0.1 and 0.8 fractions of the overall hydrogen capacity. The best fitting reaction rate model must obey the following rules; slope of the fitted line should be ~ 1 , intercept ~ 0 and $R^2 \sim 1$. Details related to the implemented rate equations are given in our previous work⁵⁰.

IR spectroscopy was performed with an Agilent Technologies Cary 630 FT-IR located in an argon filled glove box (H₂O and O₂ levels below 1 ppm). Each measurement was acquired in the transmission mode in spectral range of 650 cm⁻¹–4000 cm⁻¹ with a resolution of 4 cm⁻¹⁵⁰.

Evolved gases during the desorption reactions were analysed using a Hiden Analytical HAL 201 Mass-Spectrometer, which is coupled with a Netzsch STA 409 C Differential Thermal Analysis (DTA-MS). About 2 mg of sample was placed in a Al₂O₃ crucible that was heated from room temperature up to 300 °C in the DTA apparatus, with a heating rate of 3 °C/min. Measurements were done under 50 ml/min Ar flow.

The absorption rates and gravimetric capacities were assessed using a Sieverts apparatus (HERA Hydrogen Storage Systems, Longueuil, QC, Canada) operating on the differential pressure technique. The hydrogen gas used in the experiments had a purity of 99.999 % (5.0 H₂). The temperature and pressure conditions are provided in the figure caption for each experiment in the manuscript. The mass of sample for all the measurements was approximately 100 mg.

High resolution transmission electron microscopy (HR-TEM) observations, diffraction patterns (DP) and dark field (DF) were carried out using a Tecnai G2 microscope with an information limit of 0.12 nm and Schottky Emission gun operating at 300 kV. Samples after milling and after absorption/desorption conditions were observed. All samples were prepared into a glove box with controlled O₂ and H₂O atmosphere (<1 ppm) by dispersing the powders onto carbon grids. In order to avoid the oxidation/hydrolysis of the material at the time to introduce the grids into the microscope column, the dispersed powder on the grid was covered with a special polymeric film which does not preclude the electron interactions with the sample⁵⁷. Then, HR-TEM observations of the identified Fe zones were done. HR-TEM image processing was done with the following programs: Digital Micrograph (License no. 90294175), i-TEM (License no. A2382500, EMSIS GmbH, Münster, Germany).

X-ray absorption spectroscopy experiments at the XANES (X-ray absorption near edge structure) region of LiTi₂O₄, K-modified additive (10 wt.% K₁₋₀₄O₁₆Ti₈, 17 wt.% LiTi₂O₄, 27 wt.% LiTiO₂ and 46 wt.% K₂O₁₇Ti₈), TiO₂ anatase, as as-milled Mg-Li-5LTO, as-milled Mg-Li-5LTOK, as-milled Mg-Li-2.5LTOK, desorbed Mg-Li-2.5LTOK and reabsorbed Mg-Li-2.5LTOK samples were carried out using a R-XAS looper “in house” spectrometer from Rigaku. The measurements were performed in transmission mode around the Ti K-edge (4966 eV) in the range of energy from 4950 eV to 5030 eV at ambient temperature. The optimum amount of material for the measurements was calculated by the program XAFSMAS (version 2012/04, ALBA synchrotron, Barcelona, Spain)⁵⁸. The samples were prepared inside a glove box by mixing them with anhydrous boron nitride (powder, purity: 98 %; Sigma-Aldrich, St. Louis, Missouri, MO, USA,) in a mortar, and then pressing the mixture into pellets of 10 mm diameter. The pellets were sealed with Kapton tape (50 μm in thickness) to prevent the oxidation/hydrolysis of the samples. XAS data processing and fitting were performed by using the IFEFFIT software (version 1.2.11, University of Chicago, Chicago, IL, USA) package⁵⁹.

Results

Results obtained from the thermal behaviour, mass spectroscopy, desorption activation energy, volumetric measurements, *ex situ* PXD, *in situ* SR-PXD and infrared spectroscopy for all the compositions are presented in this section. In Table 1, the starting stoichiometric compositions of all additives were shown and details regarding the additive synthesis were discussed in the experimental section. Rietveld refinement result of the PXD data for

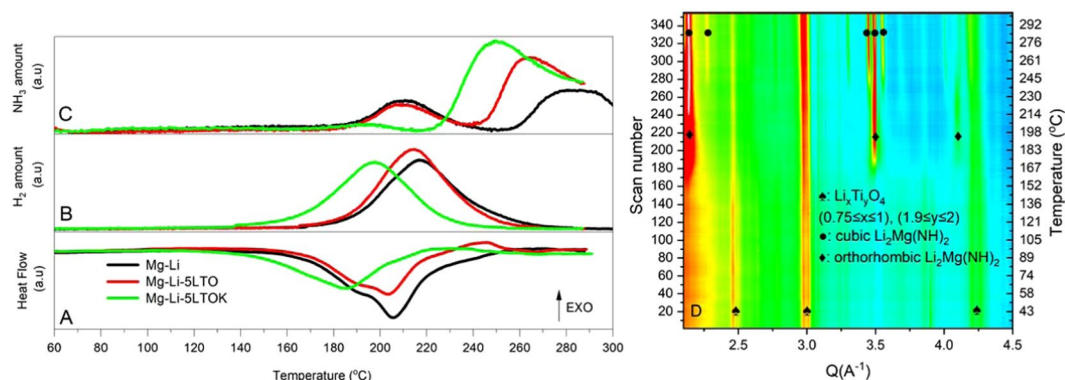


Figure 1. (A) DTA, (B,C) MS traces of as-milled samples measured in the temperature range of 60 °C–300 °C with a heating ramp of 3 °C/min and 50 ml/min Ar flow. (D) *In situ* SR-PXD data of the Mg-Li-5LTOK sample which was heated from RT to 300 °C with a heating ramp of 5 °C/min under 1 bar of Ar pressure.

the 0.5LiH + TiO₂ stoichiometric composition indicates that the additive is just composed of the LiTi₂O₄ after milling and annealing (ESI Fig. S1). In the case of the 0.5LiH + TiO₂ + 0.25KH stoichiometric composition, after the synthesis the additive is composed of 10 wt.% K_{1.04}O₁₆Ti₈, 17 wt.% of LiTi₂O₄, 27 wt.% LiTiO₂ and 46 wt.% K₂O₁₇Ti₈ (ESI Fig. S2).

First desorption/absorption performance and apparent activation energies. The thermal behaviour of as-prepared samples is presented in Fig. 1A. The DTA curve of the additive-free sample Mg-Li exhibits two endothermic events between 170 °C and 230 °C. These two events are due to desorption reactions in accordance with Eqs. 1 and 2. Temperature of the desorption peak maximum is at 205 °C. Mg-Li-5LTO sample shows a desorption trend similar to that of Mg-Li. The presence of the additive does not lead to improvement neither the onset nor the peak maximum temperatures. MS analyses of the gases (H₂ and NH₃) evolving from the two samples upon heat treatment are almost identical (Fig. 1B,C). However, the sample containing K-modified additive, Mg-Li-5LTOK, shows a reduction of 30 °C on desorption onset temperature and the peak maximum of the main thermal event. Moreover, the release of NH₃ is suppressed until 220 °C. Similar positive effects of K-based additives on the amide-hydride systems were reported previously in the literature⁴⁰. In order to understand the processes taking place upon desorption, evolution of the crystalline phases were studied by *in-situ* SR-PXD (Fig. 1D). The PXD pattern acquired at RT reveals that the reflections are ascribable to the presence of the additive (LiTi₂O₄). However, due to the broadness of the observed diffraction peaks, we cannot exclude the presence of several phases having a general formula Li_xTi_yO₄ (0.75 ≤ x ≤ 1, 1.9 ≤ y ≤ 2). This fact suggests that the additive's composition changes upon milling. The presence of reflections belonging to Li₂Mg(NH)₂ (orthorhombic phase) at around 170 °C indicates that the desorption reaction has already started, which is in good agreement with DTA analysis (Fig. 1A). The formation of the cubic Li₂Mg(NH)₂ takes place at the temperatures higher than 220 °C. This transition is expected since the phase transformation of Li₂MgN(H)₂ from the orthorhombic to the cubic structure occurs over 200 °C⁶⁰. Unfortunately, in this analysis, it was not possible to identify any crystalline potassium compounds. This implies that potassium-containing phases are either in amorphous or nanocrystalline state.

First desorption kinetics of as-milled samples are presented in Fig. 2A. Desorption of Mg-Li starts at 180 °C and 4.5 wt.% of gas is released within 120 minutes. Mg-Li-5LTO displays a similar behaviour as Mg-Li, though with a reduced capacity to 2.3 wt.% due to the presence of significant amount of additive (26 wt.%). Modifying the additive with potassium (Mg-Li-5LTOK, Mg-Li-2.5LTOK and Mg-Li-1LTOK) leads to a notable reduction on desorption onset temperature from 180 °C to 150 °C. This temperature reduction to some extent changes with the amount of LTOK additive. It is possible to observe in the inset plot of Fig. 2A that higher additive amounts lead to slightly lower onset temperatures. Additionally, DSC analyses shows that the onset temperature of Mg-Li-2.5LTOK is about 15 °C lower than that of Mg-Li-1LTOK (ESI Fig. S3). Clearly, the decrement of the amount of LTOK lead to an increase in the desorbed gas amount. As seen in Fig. 2A, Mg-Li-5LTOK desorbs 3 wt.%, whereas Mg-Li-2.5LTOK and Mg-Li-1LTOK desorbs 3.8 wt.% and 4.3 wt.%, respectively. K-containing additives, especially KH, are known to improve reaction kinetics of Mg(NH₂)₂ + LiH system^{40–42}. In order to compare our findings with the pure KH added system, Mg-Li-5K sample (Mg(NH₂)₂ + 2LiH + 0.05KH) was prepared. Despite the fact that the lowest onset temperature (135 °C) is obtained with this sample, its reaction rate is slower in comparison with the samples containing K-modified additive.

Reabsorption kinetics of Mg-Li and Mg-Li-5LTO are sluggish and require more than 10 hours to reach full capacity (Fig. 2B). On the contrary, K-modified samples absorb H₂ notably faster (Mg-Li-5LTOK within 1 hour, Mg-Li-2.5LTOK within 2.5 hours and Mg-Li-1LTOK within 2 hours). Therefore, the effect of K-modified additive on Mg-Li is clearly seen both in the absorption and desorption kinetic properties. Despite the fact that Mg-Li-1LTOK has fast H₂ absorption kinetic, the H₂ capacity is reduced from 4.3 to 3 wt. % after a single cycle. After cycling, the best sample that has a good H₂ absorption kinetic and cycling stability is Mg-Li-2.5LTOK. For this reason, we chose this sample to further investigate its cycling stability compared to Mg(NH₂)₂ + 2LiH system.

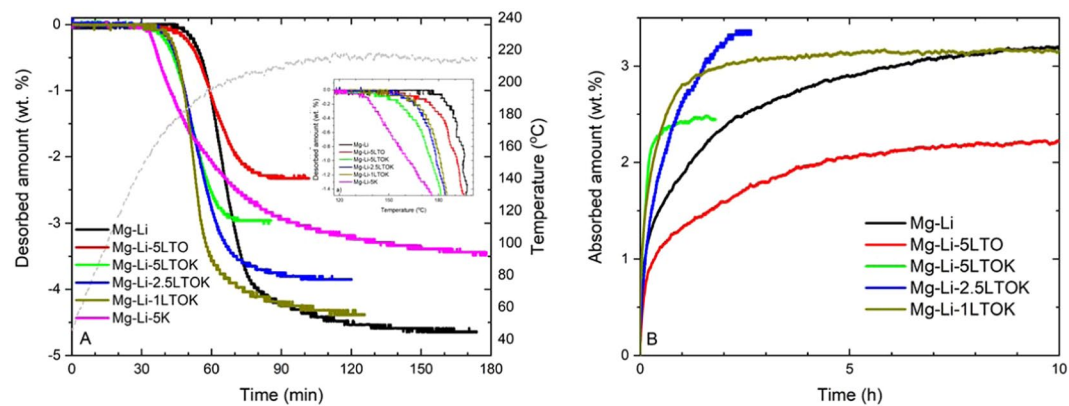


Figure 2. (A) 1st Desorption kinetics of as-milled samples (RT → 220 °C under 1 bar of H₂, 3 °C/min heating rate) (B) Reabsorption kinetics at 180 °C (isothermal) and 80 bar of H₂ pressure.

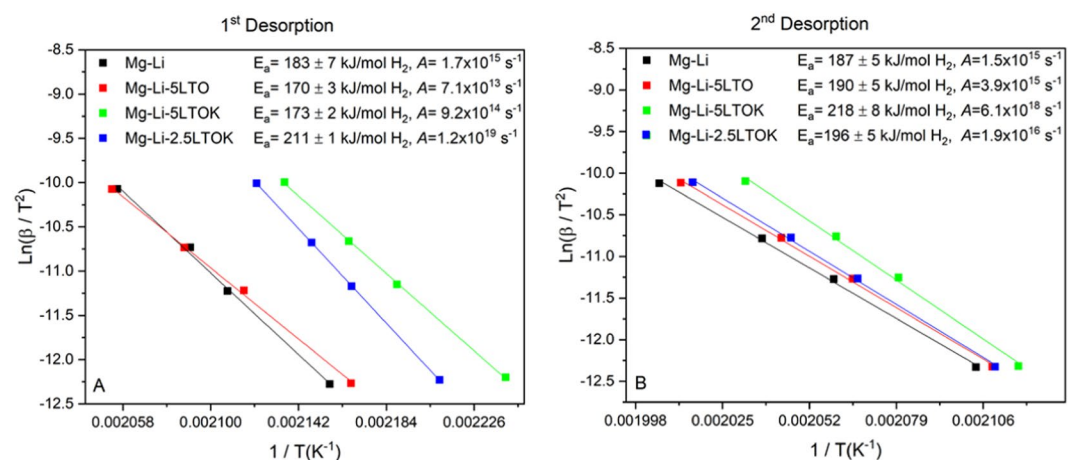


Figure 3. Kissinger plots of samples: (A) 1st desorption, (B) 2nd desorption derived from DSC curves at different heating rates (1, 3, 5 and 10 °C/min) for the calculation of the E_a .

In order to evaluate the effect of the modified additives on desorption apparent activation energy (E_a), the Kissinger method⁵⁴ was applied for the 1st and 2nd desorption reactions of the Mg-Li, Mg-Li-5LTO, Mg-Li-5LTOK and Mg-Li-2.5LTOK samples. For the calculations, the peak maximum of the main thermal event (ESI: Figs. S4–S7) was considered for the calculations of the E_a . Figure 3A,B show the Kissinger plots and values of E_a . It is possible to see that the 1st desorption reaction of Mg-Li has an activation energy of 183 ± 7 kJ/mol H₂ (Fig. 3A). The presence of the additives 5LTO and 5LTOK lowers E_a down to 170 ± 3 kJ/mol H₂ and 173 ± 2 kJ/mol H₂ respectively, as well as the frequency factor (A). On the contrary, E_a value rises to 211 ± 1 kJ/mol H₂ for the sample Mg-Li-2.5LTOK. It is worthy to note that frequency factor of this sample is considerably higher ($A = 1.2 \times 10^{19} \text{ s}^{-1}$) compared to the ones of the Mg-Li, Mg-Li-5LTO and Mg-Li-5LTOK samples.

The E_a values calculated for the 2nd desorption reactions (Fig. 3B) increase in comparison with the 1st desorption, except for Mg-Li-2.5LTOK, which decreases by nearly 15 kJ/mol. It is worthy to note that the experiments were repeated in order to confirm this trend. Taking into account the error bands (ESI – Fig. S7), the E_a values for Mg-Li, Mg-Li-5LTO and Mg-Li-2.5LTOK overlap. However, the frequency factor for Mg-Li-2.5LTOK is higher than the ones for Mg-Li and Mg-Li-5LTO. The highest values of E_a and A were measured for Mg-Li-5LTOK. It is also noticed that K-containing additives reduce the desorption peak temperature both in the 1st and 2nd desorption.

Cycling stability. In Figs. 1 and 2, it was shown that LTOK additive improves the hydrogen storage properties of the Mg(NH₂)₂ + 2LiH hydride system, i.e. reduced desorption temperature, fast reabsorption kinetic. Mg-Li-2.5LTOK sample exhibited the highest reversible H₂ storage capacity of about 3.5 wt. % (Fig. 2). Hence, this subsection presents its cycling stability/reversibility in comparison with the sample without additive, i.e. Mg-Li. Figure 4 shows the cycling stability upon 5 absorption/desorption processes for Mg-Li and Mg-Li-2.5LTOK samples. During cycling, both desorption and absorption kinetics of Mg-Li-2.5LTOK are 2 and 5 times faster, respectively, than those of Mg-Li. In addition, the hydrogen storage capacity of Mg-Li is reduced by a half after 5 cycles, from 3.4 to 1.7 wt. %, whereas the cycling process reduces only in 10% the hydrogen capacity, i.e. from 3.1 to 2.75 wt. %, in the case of Mg-Li-2.5LTOK sample. From Fig. 4B, it is observed that measurement time of 12 hours is not enough for the complete absorption in Mg-Li sample, whereas Mg-Li-2.5LTOK reaches almost equilibrium at this time.

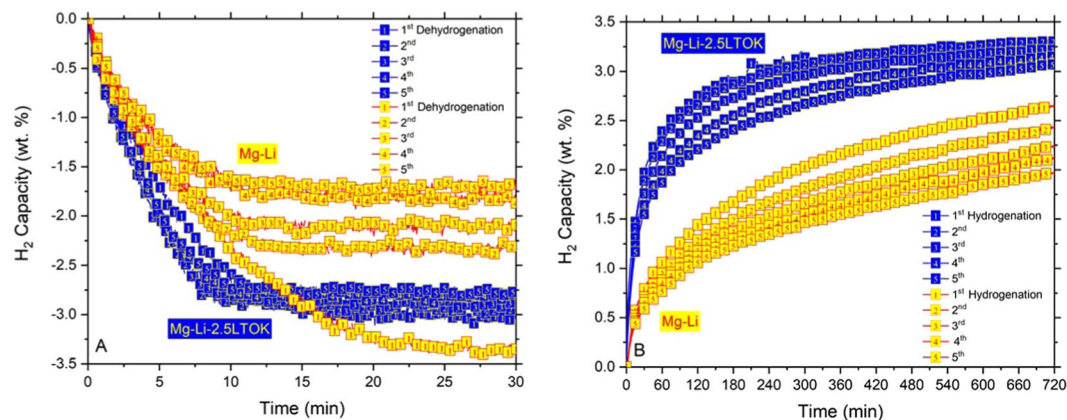


Figure 4. Reaction kinetics of Mg-Li and Mg-Li-2.5LTOK within the first 5 H₂ absorption/desorption cycles, (A) Isothermal desorption at 180 °C and 1 bar of H₂ pressure (B) Isothermal absorption at 180 °C and 80 bar of H₂.

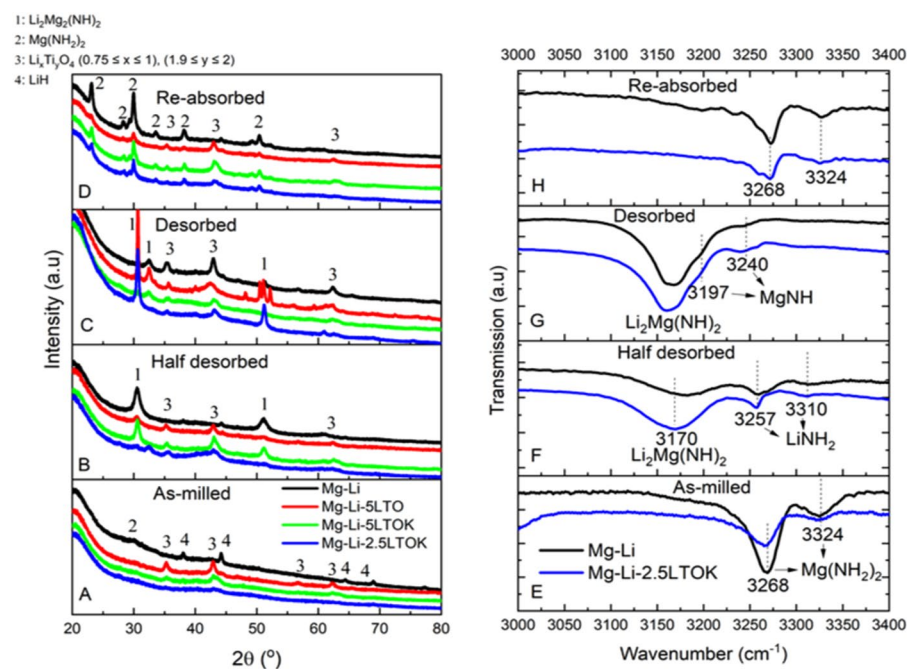


Figure 5. (A–D) PXD plots of samples at different reaction states. (E–H) Corresponding FT-IR plots of samples Mg-Li and Mg-Li-2.5LTOK. Desorption and absorption were performed under 1 bar of H₂ at 210 °C and 80 bar of H₂ pressure at 180 °C, respectively.

Initial structural analysis. First overview to the structural analysis was done with PXD and FT-IR techniques (Fig. 5A–D,E–H, respectively). PXD patterns of the samples after ball milling (Fig. 5A) exhibit broad peaks with low intensity, which can be attributed to the harsh milling conditions. As-milled Mg-Li contains cubic LiH structure with *Fm3m*(225) space group and a broad peak at $2\theta = 30^\circ$, which corresponds to the tetragonal Mg(NH₂)₂ structure with *I4₁/acd*(142) space group. Since Mg(NH₂)₂ is amorphous after intense ball milling, it can be hardly observed in PXD⁶¹. In contrast, it is more visible on the FT-IR pattern (Fig. 5E), where N-H stretching vibrations of Mg(NH₂)₂ are positioned at 3268 and 3324 cm⁻¹. When Mg-Li is half desorbed, LiNH₂ can be detected at 3257 and 3310 cm⁻¹ (Fig. 5F). Fully desorbed sample contains small bumps at 3240 and 3197 cm⁻¹, which correspond to IR signals from MgNH (Fig. 5G)⁶². LiNH₂ and MgNH products from the desorption of the sample should have a solid-solid reaction to form a ternary imide: Li₂Mg(NH)₂⁶³. PXD reflections coming from the cubic Li₂Mg(NH)₂ phase with *iba2*(45) space group are found in the half and fully desorbed samples (Fig. 5B,C). This imide is also observed by FT-IR at 3170 cm⁻¹ (Fig. 5E,G). Absorption of the desorbed Mg-Li at 180 °C leads to recrystallization of Mg(NH₂)₂ (Fig. 5D).

Regarding the additives, PXD analyses (Fig. 5A–D) reveal that in all cases Li_xTi_yO₄ compounds with $0.75 \leq x \leq 1$ and $1.9 \leq y \leq 2$ are present. In the ICSD database, it is possible to find several crystal structures

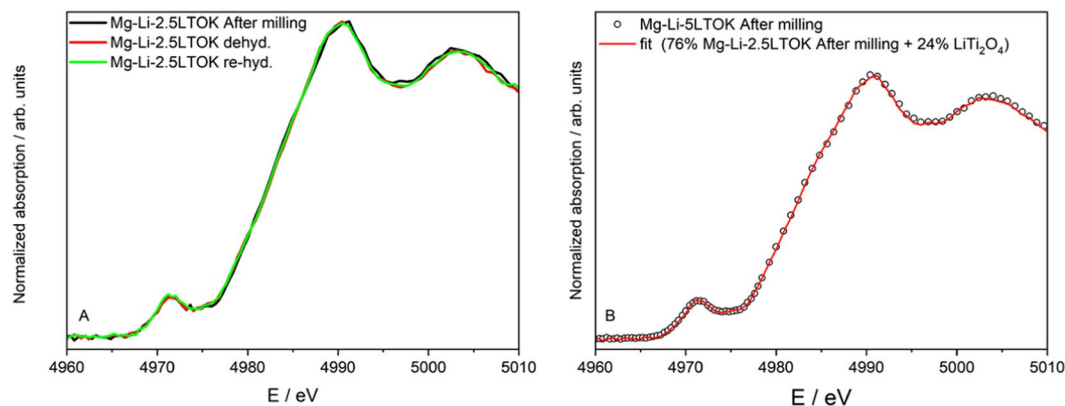


Figure 6. (A) XANES spectra at the Ti K-edge of Mg-Li-2.5LTOK after milling (black line), after dehydrogenation (red line) and after rehydrogenation (green line). (B) Linear combination fit (red line) for the XANES spectrum of Mg-Li-5LTOK (circles).

belonging to $\text{Li}_x\text{Ti}_y\text{O}_4$ that fit well with all reflections⁶⁴. These formed phases are stable and their peaks positions do not change within desorption/absorption processes. The compositions of the as-synthesized additives were already presented in the introduction of the results section (ESI Figs. S1 and S2). However, it is observed that further mechanical milling of these additives with $\text{Mg}(\text{NH}_2)_2$ and LiH leads to some changes in the additives' composition, which will be later discussed in the following section.

Discussion

In this work, microstructural and kinetic effects of $\text{Li}_x\text{Ti}_y\text{O}_z$ and K-modified $\text{Li}_x\text{Ti}_y\text{O}_z$ additives on the $\text{Mg}(\text{NH}_2)_2 + 2\text{LiH}$ system were studied. K-modified additive not only plays a role on improving the reaction kinetic behaviour (Fig. 2) and cycling stabilities (Fig. 4), but also helps lowering the desorption onset and peak temperatures (Fig. 1A) in comparison to the pristine sample (Mg-Li). Mg-Li releases NH_3 at the cycling temperature of 180 °C, which is comparably lower respect to the release of H_2 . However, the suppression of NH_3 release at this temperature was achieved by the addition of LTOK (Fig. 1C). Then, the H_2 storage capacity was optimized by tuning the amount of additive. Thus, a reversible H_2 capacity of about 3 wt. % at 180 °C was achieved for Mg-Li-2.5LTOK upon cycling (Fig. 4). FT-IR analyses carried out for the sample Mg-Li and Mg-Li-2.5LTOK after milling, after desorption and absorption (Fig. 5E–H) confirmed that the reaction pathway described in reactions (1) and (2), section 1, is not altered.

As we reported in Fig. 5, the composition of the additive after milling with $\text{Mg}(\text{NH}_2)_2$ and LiH changes. XRD analyses of the as-milled materials (Fig. 5A,D) provided a hint about the presence of stable $\text{Li}_x\text{Ti}_y\text{O}_z$ compounds ($0.75 \leq x \leq 1$ and $1.9 \leq y \leq 2$). Nevertheless, the composition of the additives in the LTOK after milling is not clear yet. Therefore, X-ray absorption spectroscopy near edge structure (XANES) technique was applied to Mg-Li-5LTO, Mg-Li-5LTOK and Mg-Li-2.5LTOK samples in order to investigate the oxidation state of Ti. The changes in the oxidation state of Ti were determined by the shift of the absorption edges of the samples. The results were compared with the measured XANES spectra of TiO_2 and LiTi_2O_4 reference materials. In Fig. 6A, the spectra of the Mg-Li-2.5LTOK after milling, desorption and reabsorption are compared. It is possible to observe that all spectra are similar, thus the nature of the LTOK additive does not change upon hydrogen interaction. It was found that the oxidation state of Ti in both additives LTO (LiTi_2O_4 ; 100 %, ESI Fig. S1) and LTOK (10 wt.% $\text{K}_{1-04}\text{O}_{16}\text{Ti}_8$, 17 wt.% of LiTi_2O_4 , 27 wt.% LiTiO_2 and 46 wt.% $\text{K}_2\text{O}_{17}\text{Ti}_8$, ESI Fig. S2) is the same (ESI Fig. S8). Durmeyer *et al.* already reported that Ti in LiTi_2O_4 has an effective valence state of +3.5⁶⁵. Thus, the effective oxidation state of Ti in LTO and LTOK additives is +3.5. Comparing the XANES spectra of the as-milled Mg-Li-5LTO, the LTO additive and anatase TiO_2 (ESI Fig. S9A), it is possible to observe a change in the position of the absorption edge towards higher energies for the Mg-Li-5LTO respect to LTO additive. Hence, this indicates that the valence state of Ti atoms in Mg-Li-5LTO is, on average, higher than +3.5 and lower than +4. A similar behaviour is observed for the Mg-Li-5LTOK sample (ESI Fig. S9A), with a slightly shift toward higher energies on the absorption edge respect to Mg-Li-5LTO. This fact suggests that a different titanium compound could be formed in the potassium-containing samples. If we compare two samples with different LTOK additive loads (Mg-Li-5LTOK and Mg-Li-2.5LTOK), the absorption edge of both samples seems to be similar, showing that the average Ti valence in this samples is very close (ESI Fig. S9B). Then, the results from the Fig. S9 show that the effective valence state of the Ti atoms in the samples slightly depends on the presence of the K-based additive. Based on the analysis above, it is possible to reproduce the Mg-Li-5LTOK spectrum with 76 % of Mg-Li-2.5LTOK and 24 % of LTO additive (LiTi_2O_4) as shown in Fig. 6B. Thus, K-modified additive in the Mg-Li-5LTOK sample is composed of 24 % of LiTi_2O_4 ($\text{Ti}^{+3.5}$) and 76 % of other species, suggesting that the effective Ti valence state is slightly smaller than the presented by the Mg-Li-2.5LTOK sample.

TEM observations and analyses were performed to determine the nature of the formed additives upon milling. Figure 7 shows bright field TEM photos (BF), diffraction patterns (DP) and tables of possible phases based on the DP and dark field images (DF), for the as-milled Mg-Li-5LTO and Mg-Li-2.5LTOK samples. The DP of as-milled samples were taken in the region showed by the BF images. Reflections from the DP are related to the

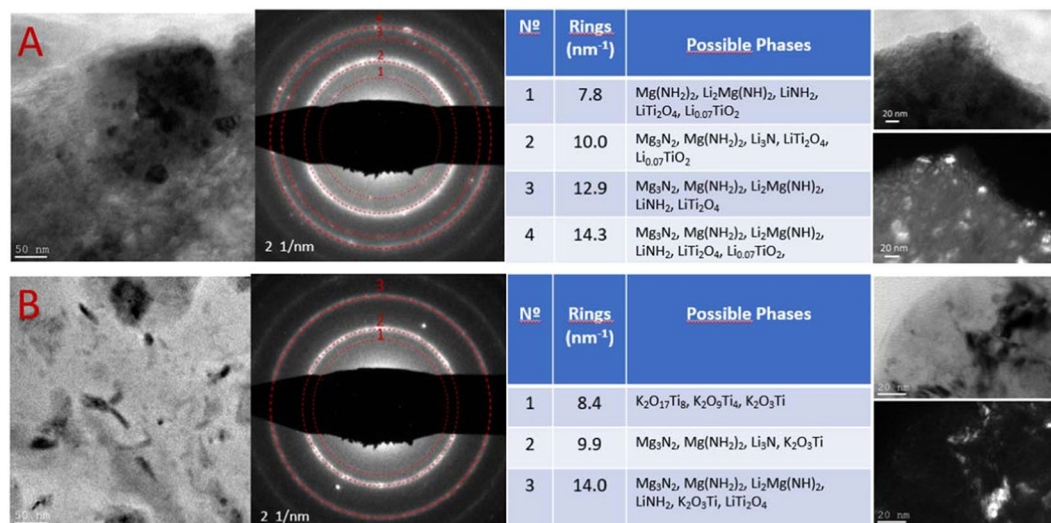


Figure 7. TEM bright field photos (BF, left), diffraction patterns (DP, middle), table for possible phases and, BF+DF set of images (right column): (A) Mg-Li-5LTO and (B) Mg-Li-2.5LTOK.

main phase of the material, Mg(NH₂)₂ compound. Due to the thickness of the rings, it is not possible to discard some intermediate (LiNH₂), product (Li₂Mg(NH)₂) and by-product (Li₃N and Mg₃N₂) species. However, these phases are not expected in the as-milled state, unless Mg(NH₂)₂ and LiH interacts during the observations prompted by the energy of the beam. It is also possible to attribute the observed reflections to species composed of Li-Ti-O (Fig. 7A) and K-Ti-O (Fig. 7B). On the one hand, species such as LiTi₂O₄ and Li_{0.07}TiO₂ are found for the Mg-Li-5LTO sample. On the other hand, species composed of K-Ti-O as well as LiTi₂O₄ are present in the Mg-Li-2.5LTOK sample. Dark field images formed from 3rd and 4th rings for Mg-Li-5LTO and from the 3rd ring for Mg-Li-2.5LTOK shows small nanoparticles in the range of 5 to 30 nm that can be attributed to the Li-Ti-O and K-Ti-O species.

In order to verify the formation of such Li-Ti-O and K-Ti-O nanoparticles, HR-TEM observation, fast Fourier transform (FFT) and crystal structure simulation analyses were performed. Figure 8 shows the HR-TEM of the as-milled Mg-Li-5LTO and as-milled Mg-Li-2.5LTOK along with its FFTs calculated in each region, and compared to simulated diffraction patterns (DPs). In the as-milled Mg-Li-5LTO (Fig. 8A), the presence of nanoparticles of Li_{0.07}TiO₂ (tetragonal) and LiTi₂O₄ (cubic) are confirmed by the structure analyses of the HR-TEM photos. For the as-milled Mg-Li-2.5LTOK (Fig. 8B), nanoparticles of K₂TiO₃ (orthorhombic) and LiTi₂O₄ (cubic) are found. Based on the position of the absorption edge of the Mg-Li-2.5LTOK sample compared to the ones from references TiO₂ and LiTi₂O₄ (Fig. S9B), we can attribute those titanium atoms in the sample has an average valence state higher than +3.5 and close to +4.

In terms of the observed improved kinetic behaviour (Fig. 2), and the calculated desorption E_a for the first and second desorption reactions (Fig. 3), we can find some unexpected results. On one hand, the Mg-Li-2.5LTOK sample clearly shows reduced onset temperature upon the first desorption and faster kinetic during the first (Fig. 2A), second and subsequent absorption/desorption cycles (Fig. 4) in comparison with the Mg-Li sample. Moreover, among the samples with additives, the Mg-Li-2.5LTOK sample exhibit higher capacity (~3 wt.%) and faster absorption kinetics (Fig. 4). On the other hand, the activation energy values are higher than the one of the material without additive, Mg-Li (Fig. 3). In order to shed light onto this fact, the kinetic constant (k) was calculated by the Arrhenius expression $k = A \cdot \exp[-E_a/RT]$ (1/s) at 180 °C, which is the cycling temperature (Fig. 4). Then, to take into account the effect of the capacity of each sample, k was multiplied by the capacity after reabsorption taken from Fig. 2B, which can be considered as the more realistic value (ESI – Table S1). As seen in Fig. 9, the desorption rate upon the first and second desorption reactions for the samples with the addition of LTOK is faster than the ones for the Mg-Li and Mg-Li-5LTO samples. However, the activation energies for LTOK containing samples are similar or higher. This behaviour can be mainly attributed to an increase in the frequency factor, making possible a more efficient contacting of the reactants on the interphase.

The faster rate of the sample with 5-mol. % LTOK during the first desorption is in agreement with the lower E_a in comparison with sample with 2.5-mol. % LTOK, suggesting a better distribution of the additive. However, during the second desorption, the beneficial effects of the larger amount of additive is lost, hinting that the additive might have agglomerated and then acting as a barrier for the reactants interactions. Moreover, adding 5-mol. % LTOK leads to a notable drop in the desorbed gas amount.

In order to further investigate the role of the additive on the system, an analysis on the rate-limiting steps⁶⁶ of Mg-Li and Mg-Li-2.5LTOK samples is carried out for the 1st, 2nd and 5th absorption/desorption kinetic curves from Fig. 4 (ESI Figs. S10–S21; Tables S2–S6). The results are summarized in Table 2. Desorption rates are limited by an interface controlled mechanism (F1: JMA, $n = 1$), while absorption rates are limited by a diffusion controlled mechanism. In the case of absorption reaction, D3 and D4 represent diffusion mechanisms as rate limiting step, but with different geometries of particles (D3: spheres and D4: different forms). Therefore, K-modified

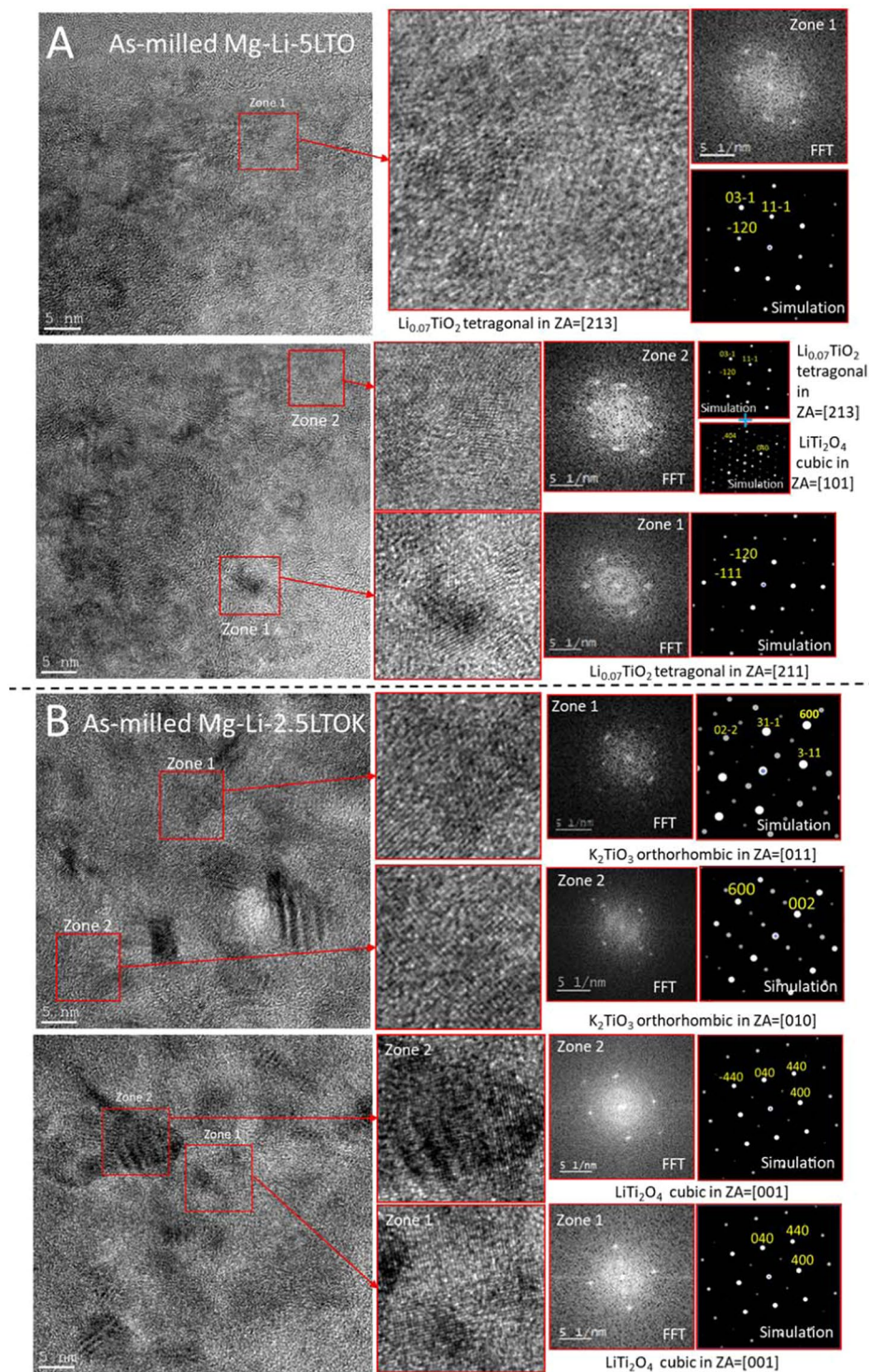


Figure 8. Characterization of the nano-sized Li-Ti-O and K-Ti-O for (A) as-milled Mg-Li-5LTO and (B) as-milled Mg-Li-2.5LTOK by means of HR-TEM. FFT was calculated in each region and compared to simulated diffraction patterns (DPs) in the adequate orientation.

additive does not change the rate-limiting step for desorption/absorption reactions. However, in both absorption and desorption mechanisms, the rate-limiting step is notably accelerated. In general, the results are in well agreement with the results obtained from our previous work, where amide/hydride molar ratio was 6/9 instead of 1/2⁵⁰.

Therefore, these outcomes suggest that the presence of the K_2TiO_3 species account for the observed improvements in the kinetic behaviour and cycling stability of the Mg-Li-2.5LTOK. Kinetic enhancements from the alkali metals and their hydrides/hydroxides/amides are still discussed, whether they modify thermodynamics of the system or they have a catalytic effect on the system^{32,37,38,41,67-70}. Catalytic activity of KH and RbH was explained

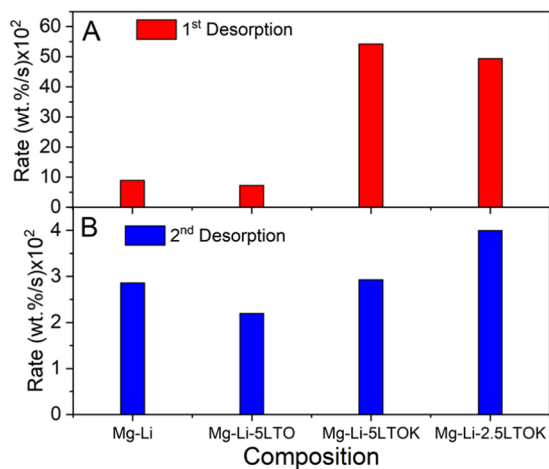


Figure 9. Reaction rate for the first and second desorption processes for the investigated samples.

Desorption	
1 st Desorption	F1
2 nd Desorption	F1
5 th Desorption	F1
Absorption	
1 st Absorption	D3
2 nd Absorption	D4
5 th Absorption	D3

Table 2. Using Sharp and Jones method^{55,56}, rate-limiting processes of samples, which were taken from isothermal cycling kinetic curves of Fig. 4. F1 : JMA, $n = 1$, Random nucleation, one-dimensional interface controlled growth. D3 : Three-dimensional diffusion, spherical particles. D4 : Three-dimensional diffusion, free geometry.

via destabilization of N-H bond due to their high electronegativity³². KH firstly reacts with $\text{Mg}(\text{NH}_2)_2$ and later metathesizes with LiH to regenerate KH⁴¹. Based on our results from *in situ* SR-PXD contour plot (Fig. 1D) together with XANES spectra (Fig. 6B), we propose that K_2TiO_3 does not take part in the reactions, but its presence can positively affect the reversible reactions of the $\text{Mg}(\text{NH}_2)_2 + 2\text{LiH}$ system due to high electronegativity of K (0.82 eV), Ti (1.54 eV) and O (3.44 eV) elements. Therefore its acts as a catalyst rather than changing the thermodynamics of the system.

Conclusions

In this work, microstructural and kinetic effects of $\text{Li}_x\text{Ti}_y\text{O}_z$ and K-modified $\text{Li}_x\text{Ti}_y\text{O}_z$ additives on the $\text{Mg}(\text{NH}_2)_2 + 2\text{LiH}$ system were studied. 5 mol. % additive containing sample Mg-Li-5LTOK reduced the desorption peak temperature of pristine sample by 30 °C and suppressed NH_3 release until 220 °C. Although Mg-Li-2.5LTOK has comparably higher apparent activation energy (211 ± 1 kJ/mol) respect to Mg-Li (183 ± 7 kJ/mol), calculated rate constant (k) value was bigger during the first and second desorption reactions which is in agreement with reaction behaviour. Orthorhombic K_2TiO_3 and cubic LiTi_2O_4 phases were detected in HR-TEM observations, where oxidation state of Ti was in accordance with XANES analysis. Based on our results from *in situ* SR-PXD plot and XANES analysis, we propose that K_2TiO_3 nanoparticles act as catalyst and they positively affect the reversible reactions of the $\text{Mg}(\text{NH}_2)_2 + 2\text{LiH}$ system due to high electronegativity of K (0.82 eV), Ti (1.54 eV) and O (3.44 eV) elements.

Data availability

The datasets generated during and/or analysed during the current study are available from the corresponding authors on reasonable request.

Received: 29 August 2019; Accepted: 27 November 2019;

Published online: 07 January 2020

References

- Schlapbach, L. & Züttel, A. Hydrogen-storage materials for mobile applications. *Nature* **414**, 353–358 (2001).
- [www.toyota.de](https://ssl.toyota.com/mirai/fcv.html). Available at: <https://ssl.toyota.com/mirai/fcv.html> (Accessed: 15th August 2019).
- Nurul, N. Z., Yaakob, Z., Lim, K. L. & Timmiati, S. N. The kinetics of lightweight solid-state hydrogen storage materials: A review. *Int. J. Hydrogen Energy* **41**, 13131–13151 (2016).

4. Milanese, C. *et al.* Solid State Hydrogen Storage in Alanates and Alanate-Based Compounds: A Review. *Metals (Basel)*. **8**, 567 (2018).
5. Wang, J., Li, H. W. & Chen, P. Amides and borohydrides for high-capacity solid-state hydrogen storage-Materials design and kinetic improvements. *Mater. Res. Soc.* **38**, 480–487 (2013).
6. Baricco, M. *et al.* SSH2S: Hydrogen storage in complex hydrides for an auxiliary power unit based on high temperature proton exchange membrane fuel cells. *J. Power Sources* **342**, 853–860 (2017).
7. Crivello, J. C. *et al.* Review of magnesium hydride-based materials: development and optimisation. *Appl. Phys. A Mater. Sci. Process.* **122**, 1–20 (2016).
8. Belosta von Colbe, J. *et al.* Application of hydrides in hydrogen storage and compression: Achievements, outlook and perspectives. *Int. J. Hydrogen Energy* **44**, 7780–7808 (2019).
9. Dornheim, M. Thermodynamics of Metal Hydrides: Tailoring Reaction Enthalpies of Hydrogen Storage Materials. In *Thermodynamics - Interaction Studies - Solids, Liquids and Gases*, 891–918, <https://doi.org/10.5772/21662> (2012).
10. Beilstein, F. & Geuther, A. Ueber das Natriumamid. *Justus Liebigs Ann. Chem.* **108**, 88–102 (1858).
11. Baumert, M. & Landolt, H. Ueber die Einwirkung des Kaliumamids auf einige organische Verbindungen. *Justus Liebigs Ann. Chem.* **111**, 1–11 (1859).
12. Schütze, M. C. B. Introduction to High Temperature Oxidation and Corrosion. By: A.S. Khanna. *Mater. Corros.* **54**, 346–347 (2003).
13. Juza, R. & Opp, K. Zur Kenntnis des Lithiumimides. *Z. anorg. allg. Chem.* **266**, 325–330 (1951).
14. Chen, P., Xiong, Z., Luo, J., Lin, J. & Lee Tan, K. Interaction of hydrogen with metal nitrides and imides. *Nature* **420**, 302–304 (2002).
15. Hu, Y. H. & Ruckenstein, E. Ultrafast reaction between LiH and NH₃ during H₂ storage in Li₃N. *J. Phys. Chem. A* **107**, 9737–9739 (2003).
16. Hu, Y. H. & Ruckenstein, E. Ultrafast reaction between Li₃N and LiNH₂ to prepare the effective hydrogen storage material Li₂NH. *Ind. Eng. Chem. Res.* **45**, 4993–4998 (2006).
17. Leng, H. Y. *et al.* New metal-N-H system composed of Mg(NH₂)₂ and LiH for hydrogen storage. *J. Phys. Chem. B* **108**, 8763–8765 (2004).
18. Xiong, Z. *et al.* Thermodynamic and kinetic investigations of the hydrogen storage in the Li-Mg-N-H system. *J. Alloys Compd.* **398**, 235–239 (2005).
19. Luo, W. & Sickafoose, S. Thermodynamic and structural characterization of the Mg-Li-N-H hydrogen storage system. *J. Alloys Compd.* **407**, 274–281 (2006).
20. Xie, L., Liu, Y., Li, G. & Li, X. Improving hydrogen sorption kinetics of the Mg(NH₂)₂-LiH system by the tuning particle size of the amide. *J. Phys. Chem. C* **113**, 14523–14527 (2009).
21. Durojaiye, T., Hayes, J. & Goudy, A. Potassium, rubidium and cesium hydrides as dehydrogenation catalysts for the lithium amide/magnesium hydride system. *Int. J. Hydrogen Energy* **40**, 2266–2273 (2015).
22. Wang, H., Cao, H., Wu, G., He, T. & Chen, P. The improved hydrogen storage performances of the multi-component composite: 2Mg(NH₂)₂-3LiH-LiBH₄. *Energies* **8**, 6898–6909 (2015).
23. Hayes, J., Durojaiye, T. & Goudy, A. Hydriding and dehydriding kinetics of RbH-doped 2LiNH₂/MgH₂ hydrogen storage system. *J. Alloys Compd.* <https://doi.org/10.1016/j.jallcom.2014.12.074> (2015).
24. Li, C., Liu, Y., Gu, Y., Gao, M. & Pan, H. Improved hydrogen-storage thermodynamics and kinetics for an RbF-doped Mg(NH₂)₂-2LiH system. *Chem. - An Asian J.* **8**, 2136–2143 (2013).
25. Li, B. *et al.* Mechanistic investigations on significantly improved hydrogen storage performance of the Ca(BH₄)₂-added 2LiNH₂/MgH₂ system. *Int. J. Hydrogen Energy* **38**, 5030–5038 (2013).
26. Demirocak, D. E. *et al.* Reversible hydrogen storage in the Li-Mg-N-H system - The effects of Ru doped single walled carbon nanotubes on NH₃ emission and kinetics. *Int. J. Hydrogen Energy* **38**, 10039–10049 (2013).
27. Li, C. *et al.* Superior dehydrogenation/hydrogenation kinetics and long-term cycling performance of K and Rb Cocatalyzed Mg(NH₂)₂-2LiH system. *ACS Appl. Mater. Interfaces* **6**, 17024–17033 (2014).
28. Pan, H. *et al.* Improved hydrogen storage kinetics of the Li-Mg-N-H system by addition of Mg(BH₄)₂. *Dalt. Trans.* **42**, 3802–3811 (2013).
29. Wang, J., Song, J., Chen, C. & Luo, D. Improvement of the dehydrogenating kinetics of the Mg(NH₂)₂/LiH materials by inducing LiBH₄. *Fusion Eng. Des.* **113**, 275–278 (2016).
30. Shahi, R. R., Raghubanshi, H., Shaz, M. A. & Srivastava, O. N. Improved hydrogen storage performance of Mg(NH₂)₂/LiH mixture by addition of carbon nanostructured materials. *Int. J. Hydrogen Energy* **38**, 8863–8871 (2013).
31. Liang, C. *et al.* Local defects enhanced dehydrogenation kinetics of the NaBH₄-added Li-Mg-N-H system. *Phys. Chem. Chem. Phys.* **13**, 314–321 (2011).
32. Durojaiye, T., Hayes, J. & Goudy, A. Rubidium hydride: An exceptional dehydrogenation catalyst for the lithium amide/magnesium hydride system. *J. Phys. Chem. C* **117**, 6554–6560 (2013).
33. Shukla, V. *et al.* Enhanced hydrogen sorption in a Li-Mg-N-H system by the synergistic role of Li₄(NH₂)₃ BH₄ and ZrFe₂. *Phys. Chem. Chem. Phys.* **19**, 9444–9456 (2017).
34. Gizer, G. *et al.* Enhancement Effect of Bimetallic Amide K₂Mn(NH₂)₄ and In-Situ Formed KH and Mn₃N on the Dehydrogenation/Hydrogenation Properties of Li-Mg-N-H System. *Energies* **12**, 2779 (2019).
35. Luo, W., Wang, J., Stewart, K., Clift, M. & Gross, K. Li-Mg-N-H: Recent investigations and development. *J. Alloys Compd.* **446–447**, 336–341 (2007).
36. Xie, L., Li, Y., Yang, R., Liu, Y. & Li, X. Superior hydrogen desorption kinetics of Mg(NH₂)₂ hollow nanospheres mixed with MgH₂ nanoparticles. *Appl. Phys. Lett.* **92**, 231910–123921 (2008).
37. Amica, G., Enzo, S., Larochette, P. A. & Gennari, F. C. Improvements in the hydrogen storage properties of the Mg(NH₂)₂-LiH composite by KOH addition. *Phys. Chem. Chem. Phys.* **20**, 15358–15367 (2018).
38. Liu, Y., Li, C., Li, B., Gao, M. & Pan, H. Metathesis reaction-induced significant improvement in hydrogen storage properties of the KF-added Mg(NH₂)₂-2LiH system. *J. Phys. Chem. C* **117**, 866–875 (2013).
39. Liang, C. *et al.* Enhanced dehydrogenation/hydrogenation kinetics of the Mg(NH₂)₂-2LiH system with NaOH additive. *Int. J. Hydrogen Energy* **36**, 2137–2144 (2011).
40. Wang, J. *et al.* Potassium-modified Mg(NH₂)₂/2LiH system for hydrogen storage. *Angew. Chemie - Int. Ed.* **48**, 5828–5832 (2009).
41. Wang, J. *et al.* Solid-solid heterogeneous catalysis: The role of potassium in promoting the dehydrogenation of the Mg(NH₂)₂/2LiH composite. *ChemSusChem* **6**, 2181–2189 (2013).
42. Li, C. *et al.* Compositional effects on the hydrogen storage properties of Mg(NH₂)₂-2LiH-xKH and the activity of KH during dehydrogenation reactions. *Dalt. Trans.* **43**, 2369–2377 (2014).
43. Li, C., Liu, Y., Yang, Y., Gao, M. & Pan, H. High-temperature failure behaviour and mechanism of K-based additives in Li-Mg-N-H hydrogen storage systems. *J. Mater. Chem. A* **2**, 7345–7353 (2014).
44. Puzskiel, J. A. *et al.* A novel catalytic route for hydrogenation-dehydrogenation of 2LiH + MgB₂: Via *in situ* formed core-shell Li₂TiO₂ nanoparticles. *J. Mater. Chem. A* **5**, 12922–12933 (2017).
45. Deprez, E. *et al.* Oxidation state and local structure of Ti-based additives in the reactive hydride composite 2LiBH₄ + MgH₂. *J. Phys. Chem. C* **114**, 3309–3317 (2010).
46. Deprez, E. *et al.* Microstructural study of the LiBH₄-MgH₂ reactive hydride composite with and without Ti-isopropoxide additive. *Acta Mater.* **58**, 5683–5694 (2010).
47. Wang, J. *et al.* The desorption kinetics of the Mg(NH₂)₂ + LiH mixture. *Int. J. Hydrogen Energy* **34**, 1411–1416 (2009).
48. Liu, Y. *et al.* Size-dependent kinetic enhancement in hydrogen absorption and desorption of the Li-Mg-N-H system. *J. Am. Chem. Soc.* **131**, 1862–1870 (2009).

49. Nayebossadri, S. Kinetic rate-limiting steps in dehydrogenation of Li-N-H and Li-Mg-N-H systems - Effects of elemental Si and Al. *Int. J. Hydrogen Energy* **36**, 8335–8343 (2011).
50. Gizer, G. *et al.* Tuning the reaction mechanism and hydrogenation/dehydrogenation properties of $6\text{Mg}(\text{NH}_2)_2\cdot 9\text{LiH}$ system by adding LiBH_4 . *Int. J. Hydrogen Energy* **44**, 11920–11929 (2019).
51. Bösenberg, U. *et al.* Characterization of metal hydrides by *in-situ* XRD. *Int. J. Hydrogen Energy* **39**, 9899–9903 (2014).
52. Hammersley, A. P. ESRF Internal Report, ESRF98HA01T, FIT2D V9.129 Reference Manual V3.1 (1998).
53. Hammersley, A. P. FIT2D: An Introduction and Overview ESRF Internal Report. *ESRF Intern. Rep.* (1997).
54. Kissinger, H. E. Reaction Kinetics in Differential Thermal Analysis. *Anal. Chem.* **29**, 1702–1706 (1957).
55. Sharp, J. H., Brindley, G. W. & Achar, B. N. N. Numerical Data for Some Commonly Used Solid State Reaction Equations. *J. Am. Ceram. Soc.* **49**, 379 (1966).
56. Jones, L. F., Dollimore, D. & Nicklin, T. Comparison of experimental kinetic decomposition data with master data using a linear plot method. *Thermochim. Acta* **13**, 240–245 (1975).
57. Puzskiel, J. *et al.* New Insight on the Hydrogen Absorption Evolution of the Mg–Fe–H System under Equilibrium Conditions. *Metals (Basel)*. **8**, 967 (2018).
58. XAFSmass, Freeware. Available online, www.cells.es/Beamlines/CLAEISS/software/xafsmass.html (accessed on 11 October 2018) (2018).
59. Ravel, B. & Newville, M. ATHENA, ARTEMIS, HEPHAESTUS: Data analysis for X-ray absorption spectroscopy using IFEFFIT. *J. Synchrotron Radiat.* **12**, 537–541 (2005).
60. Janot, R., Eymery, J. B. & Tarascon, J. M. Investigation of the processes for reversible hydrogen storage in the Li-Mg-N-H system. *J. Power Sources* **164**, 496–502 (2007).
61. Parviz, R. & Varin, R. A. Combined effects of molar ratio and ball milling energy on the phase transformations and mechanical dehydrogenation in the lithium amide-magnesium hydride $(\text{LiNH}_2 + n\text{MgH}_2)(n = 0.5\text{--}2.0)$ nanocomposites. *Int. J. Hydrogen Energy* **38**, 8313–8327 (2013).
62. Linde, V. G. & Juza, R. IR-Spektren von Amid- und Imiden zwei- und dreiwertiger Metalle gestellt; wenn das Präparat bisher noch nicht untersucht worden ist. *Z. Anorg. Allg. Chem.* **409**, 199–214 (1974).
63. Leng, H., Ichikawa, T. & Fujii, H. Hydrogen storage properties of Li-Mg-N-H systems with different ratios of $\text{LiH}/\text{Mg}(\text{NH}_2)_2$. *J. Phys. Chem. B* **110**, 12964–12968 (2006).
64. Rühl, S. Inorganic Crystal Structure Database (ICSD), A Focus on Crystallography, edited H. Müller, FIZ Karlsruhe, 6–10 (2015).
65. Drillon, M., Heintz, J. M., Kappler, J. P., Beurepaire, E. & Durmeyer, O. TiK XANES in superconducting LiTi_2O_4 and related compounds. *J. Phys. Condens. Matter* **2**, 6127–6136 (2002).
66. Pang, Y. & Li, Q. A review on kinetic models and corresponding analysis methods for hydrogen storage materials. *Int. J. Hydrogen Energy* **41**, 18072–18087 (2016).
67. Ma, L. P. *et al.* Catalytically enhanced hydrogen storage properties of $\text{Mg}(\text{NH}_2)_2 + 2\text{LiH}$ material by graphite-supported Ru nanoparticles. *J. Phys. Chem. C* **112**, 18280–18285 (2008).
68. Torre, F. *et al.* Kinetic improvement on the CaH_2 -catalyzed $\text{Mg}(\text{NH}_2)_2 + 2\text{LiH}$ system. *J. Alloys Compd.* **645**, S284–S287 (2015).
69. Luo, W., Stavila, V. & Klebanoff, L. E. New insights into the mechanism of activation and hydrogen absorption of $(2\text{LiNH}_2\text{--MgH}_2)$. *Int. J. Hydrogen Energy* **37**, 6646–6652 (2012).
70. Wang, J. *et al.* Effects of triphenyl phosphate on the hydrogen storage performance of the $\text{Mg}(\text{NH}_2)_2\text{--}2\text{LiH}$ system. *J. Mater. Chem.* **19**, 2141–2146 (2009).

Acknowledgements

This work was funded by the CAS-HZG collaborative project “RevHy” – “Study on the synthesis, structures and performances of complex hydrides systems for Reversible high capacity Hydrogen storage at low temperatures”. The authors thank CONICET (Consejo Nacional de Investigaciones Científicas y Técnicas) and Alexander von Humboldt Foundation in the frame of the post-doctoral fellowship of Dr. J. Puzskiel (Fellowship number: ARG–1187279-GF-P).

Author contributions

Conceptualization - G.G. and J.P.; formal analysis - G.G., J.P., A.S., M.M., J.M.R.L. and M.V.C.R.; investigation - G.G., J.P., M.M., T.G., J.M.R.L., J.T. and M.V.C.R.; writing - original draft preparation, G.G. and J.P.; writing, review and editing - C.P., J.P., M.M., J.M.R.L., M.D. and T.K.; supervision - C.P.

Competing interests

The authors declare no competing interests.

Additional information

Supplementary information is available for this paper at <https://doi.org/10.1038/s41598-019-55770-y>.

Correspondence and requests for materials should be addressed to G.G., C.P. or M.D.

Reprints and permissions information is available at www.nature.com/reprints.

Publisher’s note Springer Nature remains neutral with regard to jurisdictional claims in published maps and institutional affiliations.



Open Access This article is licensed under a Creative Commons Attribution 4.0 International License, which permits use, sharing, adaptation, distribution and reproduction in any medium or format, as long as you give appropriate credit to the original author(s) and the source, provide a link to the Creative Commons license, and indicate if changes were made. The images or other third party material in this article are included in the article’s Creative Commons license, unless indicated otherwise in a credit line to the material. If material is not included in the article’s Creative Commons license and your intended use is not permitted by statutory regulation or exceeds the permitted use, you will need to obtain permission directly from the copyright holder. To view a copy of this license, visit <http://creativecommons.org/licenses/by/4.0/>.

© The Author(s) 2020